RESEARCH ARTICLE
SPACE PHYSICS

Earth and Planetary Physics
10: 126–135, 2026
doi: 10.26464/epp2026006

Solar EUV flux from the triple ionosophere PhotoMeter onboard the Fengyun-3E satellite

Fang Jiang[1,2,3], Tian Mao[4], JinSong Wang[4], XiuQing Hu[4], Qian Song[4], LiPing Fu[1,2,3*], Nan Jia[1,2,3], and TianFang Wang[1,2,3]

[1]National Space Science Center, Chinese Academy of Sciences, Beijing 100190, China;

[2]Beijing Key Laboratory of Space Environment Exploration, Beijing 100190, China;

[3]Key Laboratory of Environmental Space Situation Awareness Technology, Beijing 100190, China;

[4]National Satellite Meteorological Center, China Meteorological Administration, Beijing 100081, China

Key Points:

- For the first time, TRIPM (The Triple Ionosphere Photometer) data correlated with solar zenith angle are used to retrieve solar EUV (Solar extreme ultraviolet) flux, addressing TRIPM's data application challenges.
- Our approach employs multi-model collaboration to build lookup tables; corrects N_2 Lyman-Birge-Hopfield (LBH) radiance via 135.6 nm/N_2 LBH ratio; retrieves solar EUV; prioritizes ascending orbit data (more of which is available); and excludes polar interference (by limitging data to those collected at the latitudes between 0 and ±40 degrees).
- TRIPM solar EUV results show high consistency with SOHO/SEM EUV flux. This finding broadens TRIPM's application and also confirms that photometers such as TRIPM can be los-cost, effective, EUV monitoring tools, offering a promising new approach to solar EUV flux acquisition.

Citation: Jiang, F., Mao, T., Wang, J. S., Hu, X. Q., Song, Q., Fu, L. P., Jia, N., and Wang, T. F. (2026). Solar EUV flux from the triple ionosophere PhotoMeter onboard the Fengyun-3E satellite. *Earth Planet. Phys.*, *10*(1), 126–135. http://doi.org/10.26464/epp2026006

Abstract: The Triple Ionosphere Photometer (TRIPM) is a scientific payload aboard the Fengyun-3E (FY-3E) satellite, which operates in a dawn–dusk orbit. It is primarily designed for nadir observations of airglow emissions at OI 135.6 nm and N_2 Lyman-Birge-Hopfield (LBH) bands. Due to the satellite's dawn–dusk orbital characteristics, most of TRIPM's field of view remains in a semi-illuminated condition. Therefore, compared with airglow data of the same bands acquired under purely daytime or nighttime conditions, applying TRIPM data poses greater challenges. This study presents the first attempt to use TRIPM data for retrieving solar extreme ultraviolet (EUV) flux. Our results demonstrate that by utilizing TRIPM data in regions where photoelectron excitation dominates as the primary radiation source, the solar EUV flux (denoted as Q_{EUV}) can be retrieved. Comparisons with data from the SOHO/SEM instrument reveal excellent consistency, with a seasonal correlation coefficient (R) of at least 0.95. This work thus offers a new avenue for solar EUV flux acquisition and expands the application range of TRIPM data.

Keywords: N_2 LBH band; solar EUV; thermosphere

---

1. Introduction

Solar extreme ultraviolet (EUV) radiation must be measured in space, as the upper atmosphere strongly absorbs EUV radiance. A key challenge for EUV instruments is their need for periodic recalibration, since energetic radiation causes rapid degradation of their performance (Woods et al., 2005). Notably, thermospheric emissions, such as those at OI 135.6 nm and from N_2 Lyman-Birge-Hopfield (LBH) bands, directly vary with changes in the solar EUV spectrum (Richards et al., 1994; Strickland et al., 1999; Reinisch et al., 2018). The portion of the solar spectrum driving these emissions lies below ~45 nm: photons in this range are energetic enough to generate photoelectrons, which in turn contribute to ionosphere formation and the excitation of the aforementioned thermospheric emissions. This inherent link between thermospheric airglow and solar EUV provides a viable avenue for indirect EUV retrieval. The Fengyun-3E (FY-3E) satellite launched on July 5, 2021 and operating in a dawn–dusk orbit, carries the Triple Ionosphere Photometer (TRIPM), a payload specifically designed for nadir observations of Earth's OI 135.6 nm and N_2 LBH airglow emissions (Jiang F et al., 2024, 2025). This study presents the first attempt to retrieve solar EUV flux using airglow measurements from TRIPM. For a compact, power-efficient, and cost-effective ionospheric photometer like TRIPM, the ability to generate reliable solar EUV data not only addresses the practical challenge of our currently limited low-cost EUV monitoring tools but also significantly enhances the potential

First author: F. Jiang, jiangf@nssc.ac.cn
Correspondence to: L. P. Fu, fuliping@nssc.ac.cn
Received 17 JUN 2025; Accepted 30 JUL 2025.
First Published online 29 SEP 2025.

utility and application scope of such photometers.

2. Data

2.1 TRIPM Data

For a given latitude, TRIPM observations are conducted at a fixed local time, a characteristic determined by the orbital properties of the FY-3E satellite. FY-3E operates in a sun-synchronous orbit, with its descending node occurring between 05:30 and 05:50 local time (LT, a.m.) (Zhang P et al., 2022). TRIPM comprises three independent sensors, which conduct observations of OI 135.6 nm and N_2 LBH airglow from three distinct directions. Among these, one sensor faces the nadir (directly downward), while the other two are positioned 30° to either side in the cross-track direction. At the same latitude, the local times corresponding to adjacent sensors differ by approximately 15 minutes. Based on FY-3E's orbital properties, the solar zenith angles (SZAs) for the subsatellite point's field of view are primarily distributed between 55° and 125°. Further details regarding TRIPM's design and operational principles are available in relevant literature (Wang YG et al., 2022; Jiang F et al., 2025).

Notably, under sunlit conditions, far-ultraviolet (FUV) emissions in the thermosphere, such as those at OI 135.6 nm and from N_2 Lyman-Birge-Hopfield (LBH) bands, are driven by energetic electron impacts on neutral species. Solar EUV radiation below 45 nm serves as the primary energy source for generating most of these energetic photoelectrons at sub-auroral latitudes (Richards et al., 1994; Reinisch et al., 2018). For TRIPM operated in the dawn/dusk orbit, as mentioned earlier (Zhang YL et al., 2021), as the SZA increases, solar radiation can't penetrate to lower atmospheric layers (the larger the SZA, the higher the peak emission from photoelectron-excited emission); thus, lower atmospheric layers cannot undergo excitation by the photoelectrons. Generally, most researchers agree that the ratio of 135.6 nm to N_2 LBH band radiance can be used for O/N_2 studies when the SZA does not exceed 80° (Meier, 2021). Therefore, for TRIPM, our research focuses on data collected when SZA is less than 80°. It is believed that when the SZA is less than 80°, the airglow emission originates primarily from photoelectron excitation and may thus reflect the solar EUV flux. Since the local times of the three sensors do not differ much (which means that the SZAs of the three fields of view do not differ much), the data from sensor A, which is centrally positioned, are used as representative data for analysis.

Figure 1 presents the SZA distribution corresponding to the subsatellite point's field of view recorded during the dusk–side ascending phases of TRIPM (operating in both daytime and dawn–dusk modes) for each month from March 2022 to February 2023, under magnetically quiet conditions. To avoid emission interference from polar particle precipitation, we limit our analysis to latitudes within ±40° (i.e., between 40°S and 40°N). For the same period (March 2022–February 2023) and focusing on SZAs < 80°, Figure 2 depicts the corresponding airglow intensity distribution measured by Sensor A: Panel (a) shows results for the OI 135.6 nm channel, and Panel (b) for the N_2 LBH channel. As illustrated in Figures 1 and 2, the spatial distribution of usable data (SZA < 80°, ±40° latitude) varies monthly with changes in SZA. Specifically, usable data are nearly absent in October and November, as SZAs during these months are almost always > 80°. In contrast, between March and September, usable data are concentrated primarily in the Northern Hemisphere; from December to the following February, they are distributed mainly in the Southern Hemisphere.

Correspondingly, Figure 3 presents the SZA distribution corresponding to the subsatellite point's field of view recorded during the dawn-side descending phases (in contrast to the dusk-side ascending phases of Figures 1 and 2) for the same period (March 2022–February 2023) and under magnetically quiet conditions. For the dawn-side descending phases, Figure 4 depicts the corresponding airglow intensity distribution measured by Sensor A

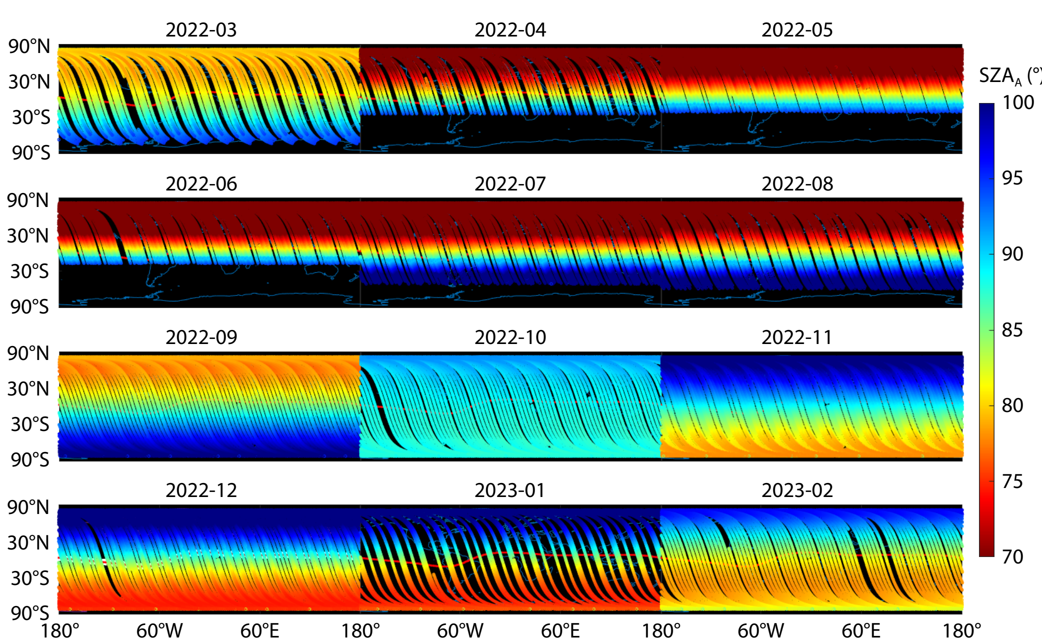

Figure 1. Solar Zenith Angle (SZA) distribution corresponding to the subsatellite point's field of view during TRIPM's dusk–side ascending phases (each month, March 2022–February 2023) under magnetically quiet conditions.

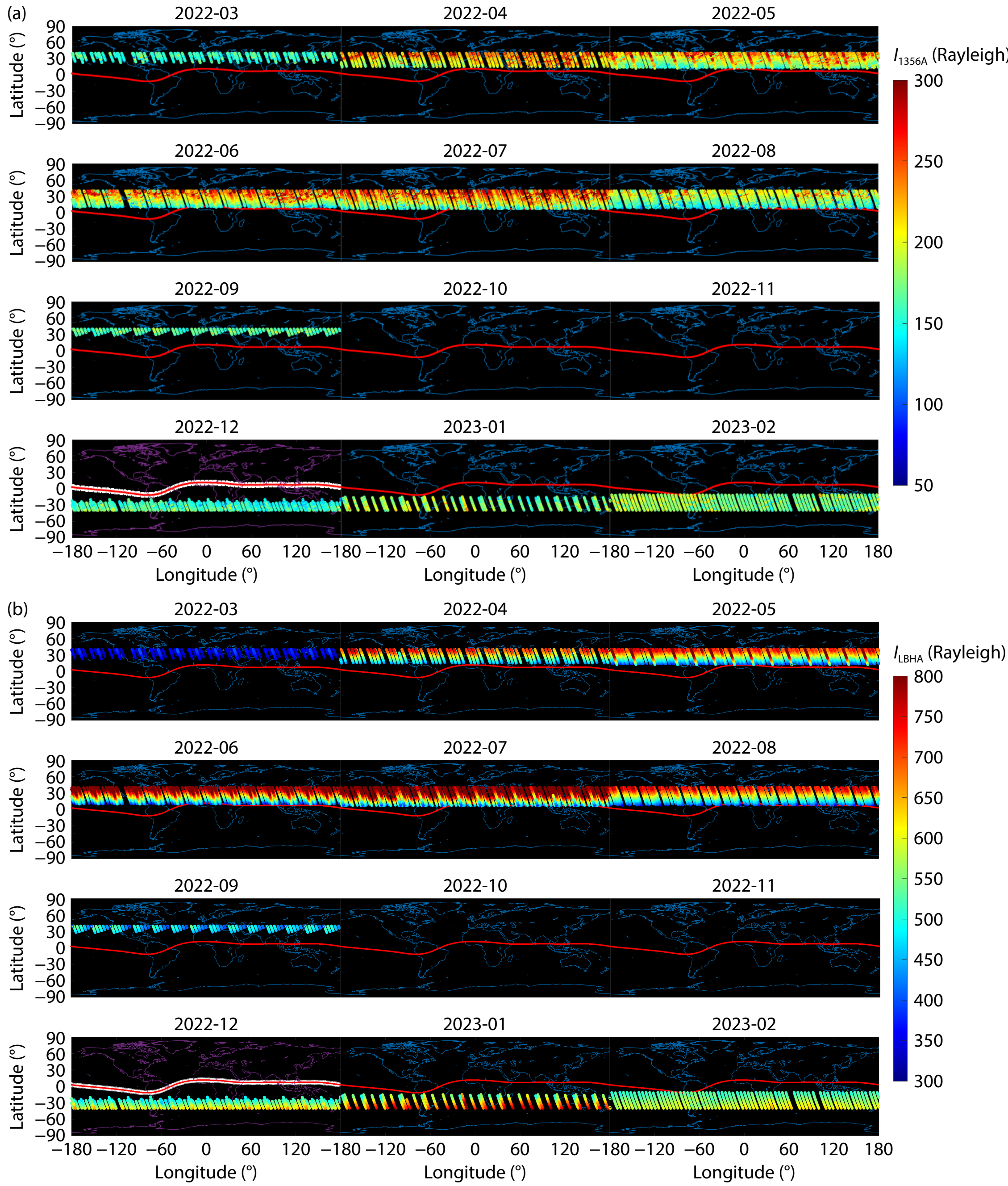

Figure 2. Airglow intensities (*I*) measured by sensor A: (a) OI 135.6 nm channel, (b) N_2 LBH band, during the ascending (dusk) phase (SZAs < 80°) corresponding to Figure 1 (March 2022–February 2023, magnetically quiet conditions).

(consistent with Figure 2's observation), filtered for SZAs < 80° and latitudes within ±40° (to avoid polar particle interference, as in Figure 2). Compared with Figure 2 (dusk-side ascending phases, same SZA and latitude constraints), usable data during the dawn-side descending phases (Figure 4) are significantly reduced: they exist only in some mid latitude regions of the Northern Hemisphere, and only from April to August.

2.2 SOHO/SEM Solar EUV Fluxes

The Solar EUV Monitor (SEM), aboard the Solar and Heliospheric Observatory (SOHO), has measured solar EUV flux continuously since 1996 (Judge et al., 1998). The SEM is equipped with two channels: a narrow-band channel (26–34 nm) and a broad-band channel (0.1–50 nm). We obtained SEM EUV data from the official repository: https://dornsifecms.usc.edu/space-sciences-center/down load-sem-data/.

Notably, the ratio of EUV flux between these two channels remains nearly constant. For this study, we therefore used the EUV flux data from the broad-band channel, as its coverage aligns with the solar EUV range relevant to our TRIPM-based retrieval.

3. Algorithm

EUV radiation below ~45 nm serves as the energy source that generates most of the energetic photoelectrons at sub-auroral latitudes. Model calculations indicate that the radiance of OI

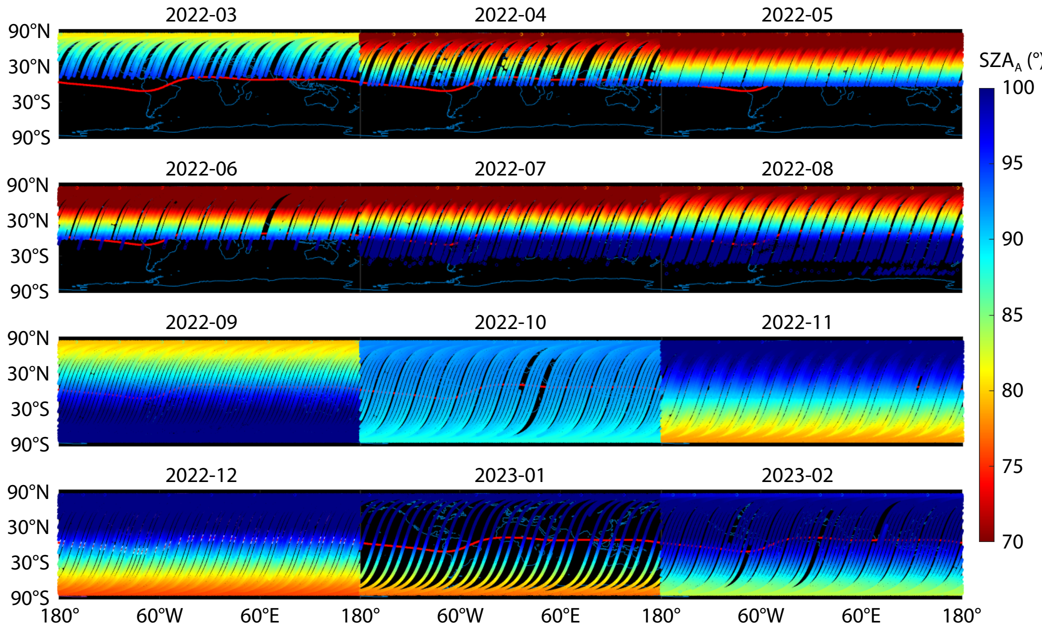

Figure 3. Solar Zenith Angle (SZA) distribution corresponding to the subsatellite point's field of view during TRIPM's dawn–side descending phases (each month, March 2022–February 2023) under magnetically quiet conditions.

135.6 nm or N_2 LBH bands is well correlated with solar EUV flux (Strickland et al., 1995). Building on this correlation, Strickland et al. (1995, 2004) developed an algorithm to estimate the integrated solar EUV flux, hereafter denoted as Q_{EUV} using OI 135.6 nm or N_2 LBH radiance. This algorithm requires a correction, either via the O/N_2 column density ratio or the OI 135.6 nm/N_2 LBH radiance ratio (135.6/LBH). Such a correction is critical because OI 135.6 nm radiance depends on both atomic oxygen (O) column density and EUV flux, while N_2 LBH radiance is influenced by N_2 column density, EUV flux, and O_2 density (i.e., radiance alone cannot isolate EUV effects from atmospheric composition changes). Notably, the column emission rates of OI 135.6 nm or N_2 LBH exhibit a linear relationship with Q_{EUV}. In contrast, the 135.6/LBH ratio is nearly invariant with Q_{EUV}. Using the Hinteregger solar spectrum (Hinteregger et al., 1981), Strickland et al. (1995) further demonstrated that, across most of their selected Q_{EUV} range and wavelength intervals, the ratio of OI 135.6 nm to N_2 LBH column emission rates remains approximately constant. This constancy allows unambiguous attribution of observed 135.6/LBH variations to changes in atmospheric composition (e.g., O/N_2) rather than solar EUV input. To construct the lookup tables, we first selected a reference atmosphere and established a two-dimensional grid defined by the O density scaling factor (f_O) and SZA. In this study, we adopted the Naval Research Laboratory Mass Spectrometer and Incoherent Scatter Radar Extended Model (NRLMSISE-00) (Picone et al., 2002), a physically realistic atmospheric model. As noted by Strickland et al. (1995), the choice of reference atmosphere exerts an insignificant influence on the lookup tables, provided the atmosphere is physically plausible. By adjusting the range of f_O (a scaling factor for O density in the reference atmosphere), we derived the corresponding O/N_2 column density ratio. For each f_O value, we constructed a SZA grid spanning 0°–88°. The choice of solar spectrum also has a weak impact on the lookup tables, and this insensitivity arises because the intensity ratio of OI 135.6 nm to N_2 LBH bands (135.6/LBH) remains effectively unchanged across different solar spectra. To define the solar spectrum, we set the $F_{10.7}$ flux (a proxy for solar activity) in the solar model, which allowed us to obtain the corresponding Hinteregger solar spectrum (Hinteregger et al., 1981). For the lookup tables tailored to TRIPM data, we adopted the Hinteregger spectrum corresponding to an $F_{10.7}$ value of 70 solar flux units (s.f.u.).

To calculate column emission rates and spectral radiances as functions of the O/N_2 column density ratio and SZA (for the input ranges described earlier), we employed the Atmospheric Ultraviolet Radiance Integrated Code (AURIC) (Strickland et al., 1999). AURIC integrates two key components to support its calculations: the NRLMSISE-00 atmospheric model (Picone et al., 2002) and the solar model discussed previously. These components are nested within AURIC to provide essential inputs: NRLMSISE-00 defines the reference atmospheric profile, while the solar model specifies the solar spectrum. Each module of AURIC operates under the control of dedicated input files. Methodologically, AURIC uses a multi-stream transport solution to solve the electron transport equation, a critical step for accurately modeling electron-driven radiance. For electron impact on atomic O, multiple scattering effects are incorporated into the column emission rates; this is achieved through the transport equation formulation and the embedded REDISTER model (Gladstone, 1982, 1988), a specialized code for solving radiative transport problems.

On the one hand, because the change in the N_2 column density variation is much smaller than that in the O column density, and on the other hand, to avoid the contamination of data by the contribution of 135.6 nm radiative recombination, the N_2 LBH radiance in this paper is used to estimate the solar EUV flux Q_{EUV}, corrected by 135.5/LBH. A two-dimensional array of N_2 LBH radiance versus 135.5/LBH and SZA is used to determine Q_{EUV}. In order to get quantitative 135.5/LBH values, a number of AURIC simulations were performed by adjusting different O density scaling factors (f_O) in atmospheric profiles from the MISIS model. A fixed solar $F_{10.7}$ flux (70 s.f.u), nadir viewing geometry, and a fixed solar

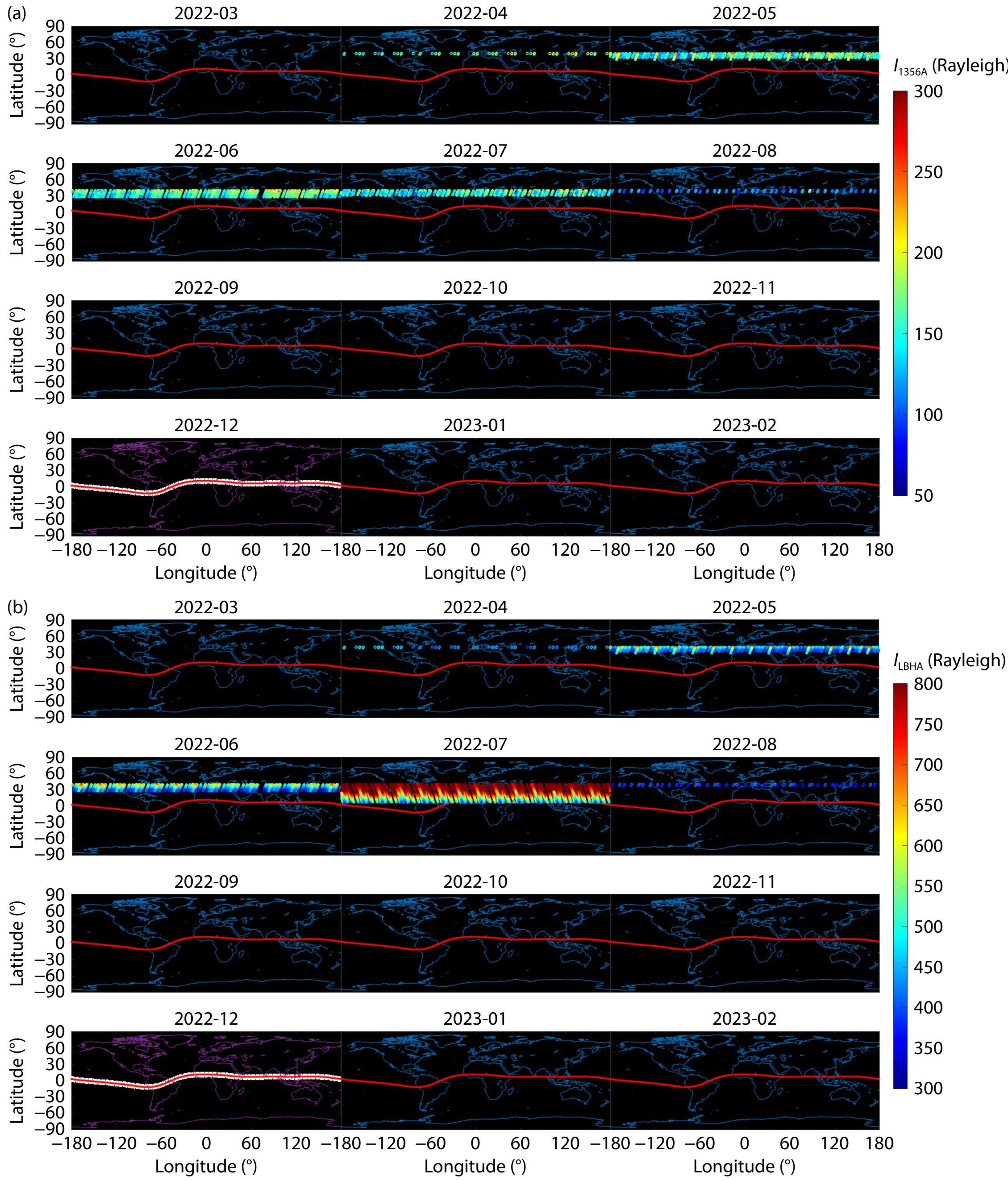

Figure 4. Airglow intensities measured by sensor A: (a) OI 135.6 nm channel, (b) N_2 LBH band, during dawn-side descending phases (SZAs < 80°, ±40° latitudes) corresponding to Figure 3 (March 2022–February 2023, magnetically quiet conditions).

zenith angle are assumed. Four *Ap* values (32, 42, 51,164) are used to drive the MISIS model. A range of N_2 LBH and the corresponding 135.5/LBH values are calculated from the storm time atmospheric profiles with scalings of the O density profile (Picone et al., 2002). Each AURIC run produces a spectrum between 105.0 and 900.0 nm with a wavelength resolution of 0.1 nm. The spectrum is then folded with the TRIPM sensor A response curve (Jiang F et al., 2024) to get the simulated 135.6 nm and N_2 LBH channel intensity in counts. The intensity in Rayleighs for each channel was derived by instrument sensitivity for the respective channel. Figure 5 shows a plot of the ratios of the simulated TRIPM sensor A 135.6 nm and N_2 LBH intensities versus the N_2 LBH intensities in Rayleighs at four solar zenith angels (SZA = 57.8°, 67.4°, 77.5°, 86.6°).

Given 135.5/LBH, Q_{EUV} may be obtained from N_2 LBH. Figure 5 show the intensities as functions of 135.5/LBH. All calculations in Figure 5 were carried out for a single solar EUV spectrum whose Q_{EUV} value is 1.06 ergs cm^{-2} s^{-1}. This is displayed in the Figure as Q_{EUV}^{ref}. I_m and I_c are the measured and calculated intensities of N_2 LBH. I_c is obtained from Figure 5 for the measured 135.6/LBH value and the SZA value appropriate to the data. Since a proportional relationship exists between intensity and Q_{EUV} for given 135.6/LBH and SZA values (Strickland et al., 1995), Q_{EUV} is then obtained from

$$Q_{EUV} = (I_m/I_c)Q_{EUV}^{ref}.$$

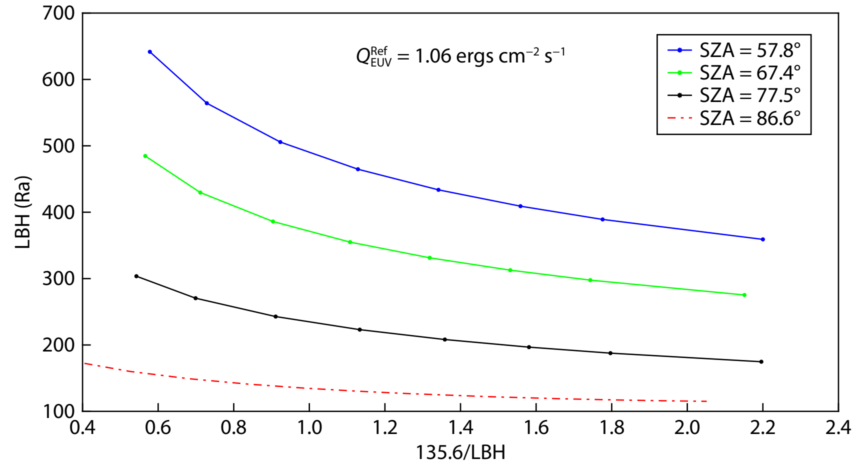

Figure 5. Nadir-viewed N_2 Lyman-Birge-Hopfield (LBH) band radiance (in rayleighs) vs. OI 135.6 nm/N_2 LBH ratio (135.6/LBH) for SZAs of 57.8°–86.6° (all results from the same solar EUV spectrum with Q_{EUV} value indicated in the figure).

4. Results

The inversion was performed using the data measured during the ascending orbit phase of TRIPM since the amount of available data during the ascending orbit phase is more than that during the descending orbit phase according to the satellite's orbital characteristics. The available data (with solar zenith angle less than 80°) mainly cover the Northern Hemisphere from the second half of March to the first half of September, and the Southern Hemisphere in January–February and December, as shown in Figure 2. Q_{EUV} quantifies solar energy input and is thus geospatially invariant; therefore, Q_{EUV} calculations for simultaneously observed but geographically separated locations should yield nearly identical values. Figure 6 presents the comparison between the average of daily per-orbit Q_{EUV} and the corresponding period SEM EUV flux

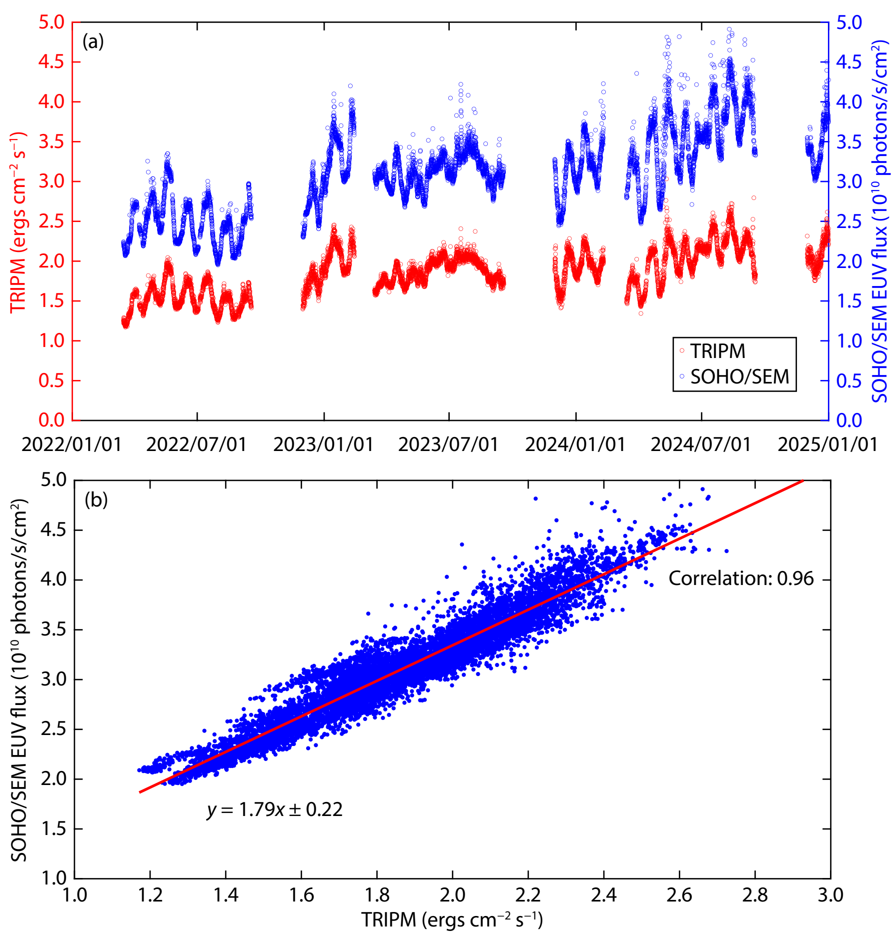

Figure 6. (a) Temporal distribution of daily averages: SOHO/SEM EUV flux (blue dots) and TRIPM-derived Q_{EUV} (red dots); (b) Scatter plot of TRIPM-derived Q_{EUV} vs. SOHO/SEM EUV flux with a linear fit (red line), March 2022–December 2024.

average value from March 2022 to December 2024. As can be seen from the Figure 6a, the Q_{EUV} value from TRIPM closely follow the changes in the EUV values (red dots) with SOHO/SEM daily EUV values (blue dots). The correlation coefficient between TRIPM and SOHO/SEM data is 0.96 as shown in Figure 6b.

Since the observational coverage of TRIPM varies seasonally, based on the data from the ascending orbit phase between March 2022 to December 2024, the correlation between TRIPM Q_{EUV} and SOHO/SEM EUV data was further evaluated seasonally. The evaluation results can be seen in Figures 7–10, which respectively present the temporal distribution of TRIPM Q_{EUV} and SOHO/SEM EUV data, as well as their correlations, for spring (March, April,

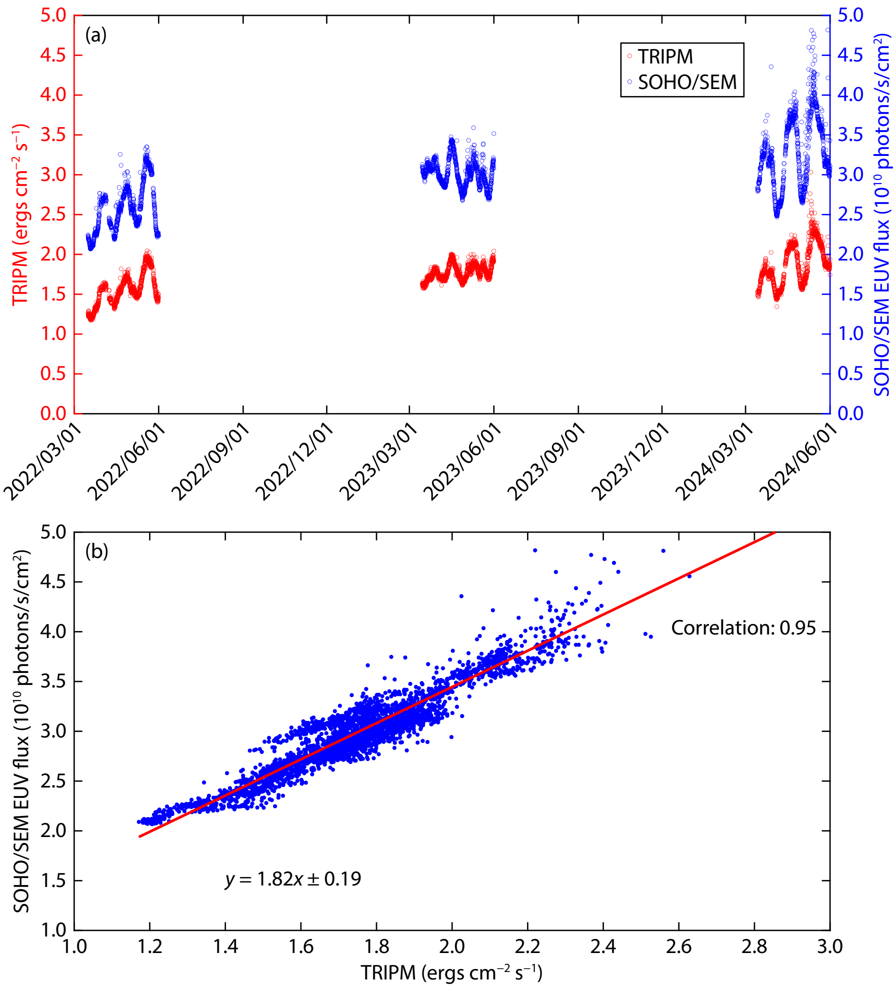

Figure 7. (a) Temporal distribution of daily averages: SOHO/SEM EUV flux (blue dots) and TRIPM-derived Q_{EUV} (red dots); (b) Scatter plot of TRIPM-derived Q_{EUV} vs. SOHO/SEM EUV flux with a linear fit (red line), spring (March–May), March 2022–December 2024

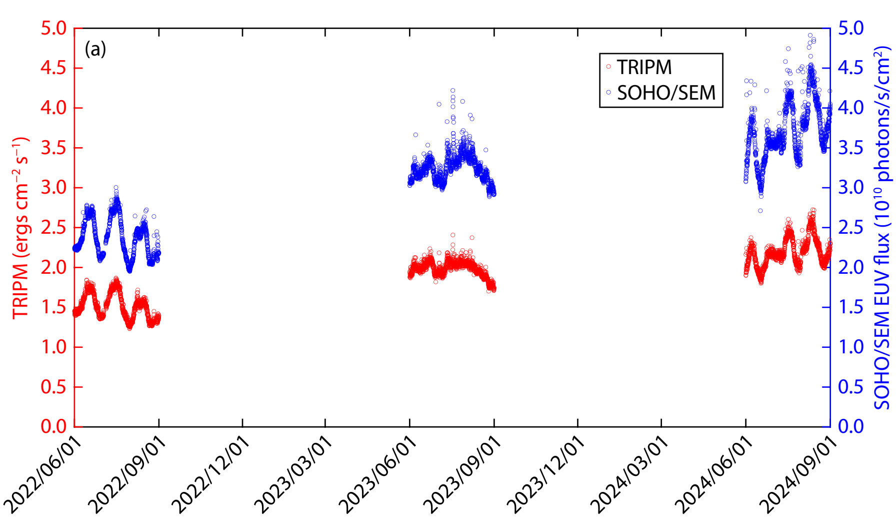

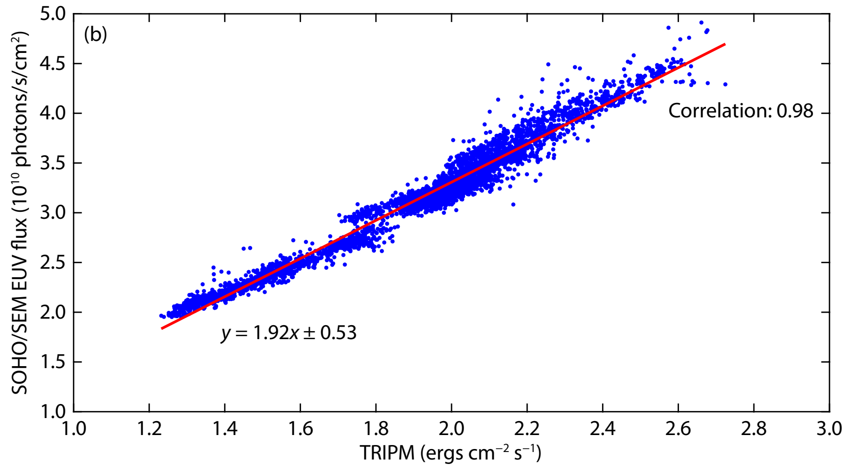

Figure 8. (a) Temporal distribution of daily averages: SOHO/SEM EUV flux (blue dots) and TRIPM-derived Q_{EUV} (red dots); (b) Scatter plot of TRIPM-derived Q_{EUV} vs. SOHO/SEM EUV flux with a linear fit (red line), summer (June–August), March 2022–December 2024.

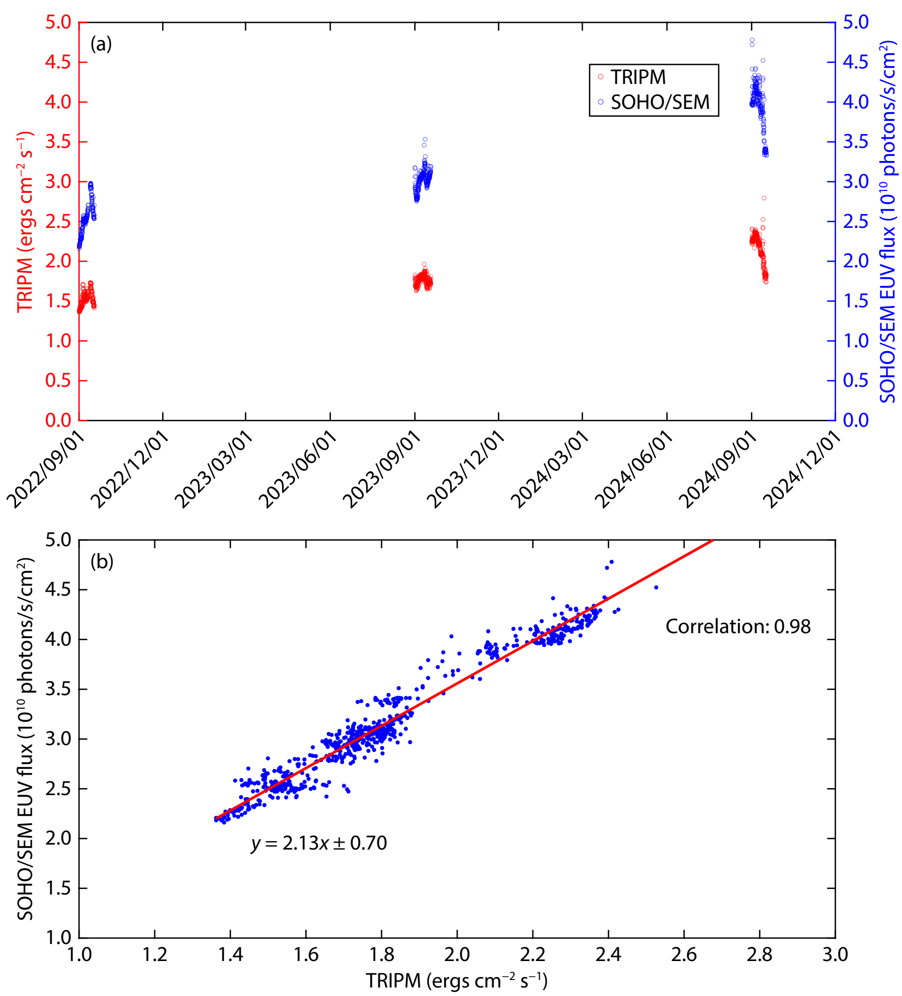

Figure 9. (a) Temporal distribution of daily averages: SOHO/SEM EUV flux (blue dots) and TRIPM-derived Q_{EUV} (red dots); (b) Scatter plot of TRIPM-derived Q_{EUV} vs. SOHO/SEM EUV flux with a linear fit (red line), autumn (only September), March 2022–December 2024.

May), summer (June, July, August), autumn (but only September, as mentioned earlier, when the solar zenith angle is less than 80°; there are no available data for November and December), and winter (December, January, February) seasons. As can be seen from panels (a) of Figures 7–10, the Q_{EUV} value from TRIPM closely follow the changes in the EUV values (red dots) with SOHO/SEM daily EUV values (blue dots). The correlation coefficient between TRIPM and SOHO/SEM data exceeds 0.95, as shown in panels (b)

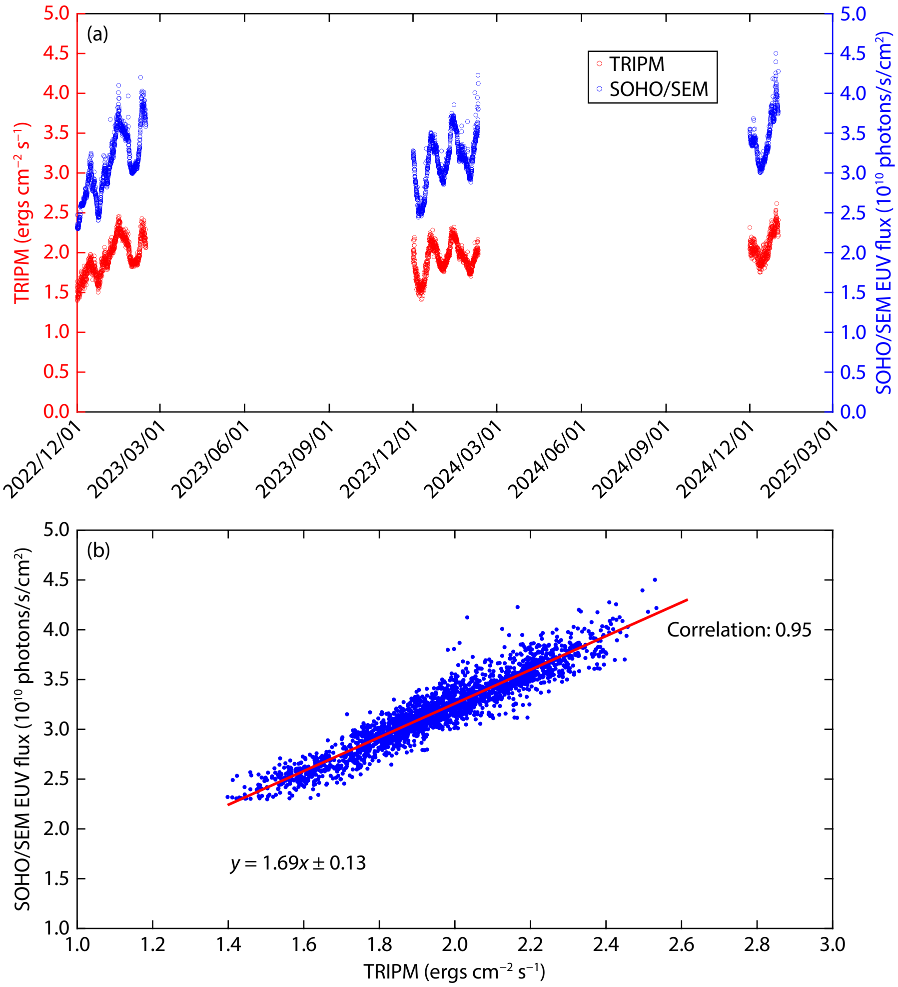

Figure 10. (a) Temporal distribution of daily averages: SOHO/SEM EUV flux (blue dots) and TRIPM-derived Q_{EUV} (red dots); (b) Scatter plot of TRIPM-derived Q_{EUV} vs. SOHO/SEM EUV flux with a linear fit (red line), winter (December–February, cross-year), March 2022–December 2024.

of Figures 7–10.

5. Conclusions

This paper estimates the solar EUV flux using TRIPM data collected when TRIPM was sunlit and the solar zenith angle was less than 80°. Both the derivation of the O/N_2 and solar EUV flux using the 135.6 nm and N_2 LBH radiance are based on photoelectron excitation. Regarding orbital characteristics, TRIPM onboard the early morning satellite FY-3E obtained the distribution of O/N_2 with only partial latitude coverage. However, solar EUV flux is a time-dependent energy input that is independent of geographical distribution. That the usable data cover only some latitudes therefore does not affect acquisition of accurate solar EUV flux. The results presented here show that the TRIPM Q_{EUV} is well correlated with the solar EUV flux observed by SOHO/SEM. This study broadens the scope of applications to which TRIPM data are likely to be suited and confirms that in the absence of direct EUV data, simple and low-cost filtered photometer instruments like TRIPM can serve as useful means of providing EUV monitoring.

Acknowledgments

This work was supported financially by National Natural Science Foundation of China (Grant No. 42174226, 42474239), National Key Research and Development Program (2022YFF0503901), and China Meteorological Administration 'Ionospheric Forecast and Alerting' Youth Innovation Team (CMA2024QN09).

References

Gladstone, G. R. (1982). Radiative transfer with partial frequency redistribution in inhomogeneous atmospheres: Application to the Jovian Aurora. *J. Quant. Spectrosc. Radiat. Transf.*, *27*(5), 545–556. https://doi.org/10.1016/0022-4073(82)90107-8

Gladstone, G. R. (1988). UV resonance line dayglow emissions on Earth and Jupiter. *J. Geophys. Res.: Space Phys.*, *93*(A12), 14623–14630. https://doi.org/10.1029/JA093iA12p14623

Hinteregger, H. E., Fukui, K., and Gilson, B. R. (1981). Observational, reference and model data on solar EUV, from measurements on AE-E. *Geophys. Res. Lett.*, *8*(11), 1147–1150. https://doi.org/10.1029/GL008i011p01147

Jiang, F., Mao, T., Fu, L. P., and Wang, J. S. (2024). Triple Ionosophere PhotoMeter onboard Fengyun-3E satellite: Data validation and ionosphere information extraction. *Adv. Space Res.*, *74*(8), 3612–3627. https://doi.org/10.1016/j.asr.2024.06.079

Jiang, F., Mao, T., Wang, J. S., Hu, X. Q., Zhang, X. X., Fu, L. P., Jia, N., and Wang, T. F. (2025). Separation of the ionospheric and thermospheric contributions in the data from the Triple Ionosphere PhotoMeter onboard the Feng-Yun 3E satellite. *Sci. China Earth Sci.*, *68*(1), 172–184. https://doi.org/10.1007/s11430-024-1451-y

Judge, D. L., McMullin, D. R., Ogawa, H. S., Hovestadt, D., Klecker, B., Hilchenbach, M., Möbius, E., Canfield, L. R., Vest, R. E., … Wurz, P. (1998). First solar EUV irradiances obtained from SOHO by the CELIAS/SEM. *Sol. Phys.*, *177*(1), 161–173. https://doi.org/10.1023/A:1004929011427

Meier, R. R. (2021). The thermospheric column O/N_2 ratio. *J. Geophys. Res.: Space Phys.*, *126*(3), e2020JA029059. https://doi.org/10.1029/2020JA029059

Picone, J. M., Hedin, A. E., Drob, D. P., and Aikin, A. C. (2002). NRLMSISE-00 empirical model of the atmosphere: Statistical comparisons and scientific issues. *J. Geophys. Res.: Space Phys.*, *107*(A12), SIA 15-1–SIA 15-16. https://doi.org/10.1029/2002JA009430

Reinisch, B. W., Dandenault, P. B., Galkin, I. A., Hamel, R., and Richards, P. G. (2018). Investigation of the electron density variation during the 21 August 2017 solar eclipse. *Geophys. Res. Lett.*, *45*(3), 1253–1261. https://doi.org/10.1002/2017GL076572

Richards, P. G., Fennelly, J. A., and Torr, D. G. (1994). EUVAC: A solar EUV flux model for aeronomic calculations. *J. Geophys. Res.: Space Phys.*, *99*(A5), 8981–8992. https://doi.org/10.1029/94JA00518

Strickland, D. J., Evans, J. S., and Paxton, L. J. (1995). Satellite remote sensing of thermospheric O/N_2 and solar EUV: 1. theory. *J. Geophys. Res.: Space Phys.*, *100*(A7), 12217–12226. https://doi.org/10.1029/95JA00574

Strickland, D. J., Bishop, J., Evans, J. S., Majeed, T., Shen, P. M., Cox, R. J., Link, R., and Huffman, R. E. (1999). Atmospheric ultraviolet radiance integrated code (AURIC): theory, software architecture, inputs, and selected results. *J. Quant. Spectrosc. Radiat. Transf.*, *62*(6), 689–742. https://doi.org/10.1016/S0022-4073(98)00098-3

Strickland, D. J., Lean, J. L., Meier, R. R., Christensen, A. B., Paxton, L. J., Morrison, D., Craven, J. D., Walterscheid, R. L., Judge, D. L., and McMullin, D. R. (2004). Solar EUV irradiance variability derived from terrestrial far ultraviolet dayglow observations. *Geophys. Res. Lett.*, *31*(3), L03801. https://doi.org/10.1029/2003GL018415

Wang, Y. G., Fu, L. P., Jiang, F., Hu, X. Q., Liu, C. B., Zhang, X. X., Li, J. W., Ren, Z. P., He, F. … Mao, T. (2022). Far-ultraviolet airglow remote sensing measurements on Feng Yun 3-D meteorological satellite. *Atmos. Meas. Tech.*, *15*(5), 1577–1586. https://doi.org/10.5194/amt-15-1577-2022

Woods, T. N., Eparvier, F. G., Bailey, S. M., Chamberlin, P. C., Lean, J., Rottman, G. J., Solomon, S. C., Tobiska, W. K., and Woodraska, D. L. (2005). Solar EUV experiment (SEE): Mission overview and first results. *J. Geophys. Res.: Space Phys.*, *110*(A1), A01312. https://doi.org/10.1029/2004JA010765

Zhang, P., Hu, X. Q., Lu, Q. F., Zhu, A. J., Lin, M. Y., Sun, L., Chen, L., and Xu, N. (2022). Fy-3E: The first operational meteorological satellite mission in an early morning orbit. *Adv. Atmos. Sci.*, *39*(1), 1–8. https://doi.org/10.1007/s00376-021-1304-7

Zhang, Y. L., Paxton, L. J., and Schaefer, R. (2021). Ionospheric and thermospheric contributions in TIMED/GUVI O 135.6 nm radiances. *J. Geophys. Res.: Space Phys.*, *126*(9), e2021JA029333. https://doi.org/10.1029/2021JA029333